Nano Research

Open Access

Research Article

Interlayer-confined dual sites in a doped graphene/MoS_2 bilayer: Synergistic effects and active site switching for boosted electrochemical nitrogen reduction

Guanping Wei[1], Zhizhi Jiang[1,2], Xijun Wang[3,4] ✉, Tiantian Hao[1], Lingli Liu[1], Zongchang Mao[1], Ling Zhu[1], Xin Xu[5] ✉, Junjie Mao[6] ✉, and Shaobin Tang[1,2] ✉

[1] *Jiangxi Provincial Key Laboratory of Synthetic Pharmaceutical Chemistry, College of Chemistry and Materials, Gannan Normal University, Ganzhou 341000, China*
[2] *Engineering Research Center of Bamboo Advanced Materials and Conversion of Jiangxi Province, Gannan Normal University, Ganzhou 341000, China*
[3] *Hefei National Research Center for Physical Sciences at the Microscale, University of Science and Technology of China, Hefei 230026, China*
[4] *State Key Laboratory of Precision and Intelligent Chemistry, University of Science and Technology of China, Hefei 230026, China*
[5] *Collaborative Innovation Center of Chemistry for Energy Materials, Shanghai Key Laboratory of Molecular Catalysis and Innovative Materials, MOE Key Laboratory of Computational Physical Sciences, Department of Chemistry, Fudan University, Shanghai 200438, China*
[6] *Key Laboratory of Functional Molecular Solids, Ministry of Education, College of Chemistry and Materials Science, Anhui Normal University, Wuhu 241002, China*

Cite this article: *Nano Research*, **2026**, *19*, 94908724. https://doi.org/10.26599/NR.2026.94908724

ABSTRACT: Single-atom catalysts (SACs) with a TM-N_4-C structure, where a transition metal (TM) atom is embedded in nitrogen-doped graphene, have emerged as promising electrocatalysts for electrochemical nitrogen reduction reaction (eNRR). However, their performance is often limited by weak N_2 adsorption and insufficient activation of the inert N≡N bond. In this work, we propose a novel bilayer catalyst architecture, Mn-N_4-C/MoS_2-TM, by vertically integrating the Mn-N_4-C site with sulfur vacancies (V_s) on the MoS_2 basal plane, where TM dopants are anchored at the V_s sites (denoted as MoS_2-TM). Using first-principles simulations, we investigated the eNRR performance within the interlayer space of this hybrid system. Our results reveal that the confined interlayer region with the dual active site of Mn-N_4-C and MoS_2-TM acts as an efficient nano-reactor, working synergistically to enhance N_2 adsorption and activation. Notably, during catalysis, the active site dynamically shifts between the Mn-N_4-C and MoS_2-TM sites for binding key reaction intermediates, significantly lowering the energy barrier of the potential-determining step, thereby promoting the conversion of N_2 to NH_3. Mechanistic analyses identify Mn-N_4-C/MoS_2-TM (TM = Mn, Tc, and Ag) as particularly promising eNRR catalysts, exhibiting a low limiting potential of −0.3 V and a maximum kinetic barrier of 0.75 eV. Furthermore, we developed a novel descriptor, $\varphi = \sqrt{\theta_d \times X_{TM}}$, based solely on intrinsic material properties (i.e., the number of d electrons (θ_d) and the electronegativity (X_{TM})) of the TM dopants, which accurately predict eNRR activity across the series. This work presents a unique strategy for rational design of dual site catalysts, opening a new avenue for efficient eNRR electrocatalysts.

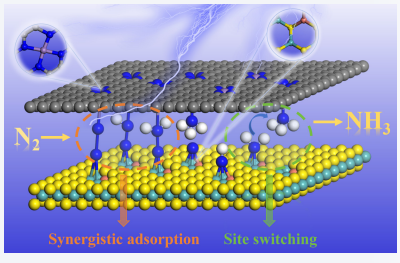

KEYWORDS: dual sites, N_2 reduction reaction, confinement effect, site switching, first-principles calculations

1 Introduction

Ammonia is an indispensable chemical feedstock for industry and agriculture, making its synthesis a cornerstone of modern society [1, 2]. Currently, industrial ammonia production predominantly relies on the Haber–Bosch process, which consumes massive energy and emits significant carbon due to its thermochemical conversion under harsh high-temperature and high-pressure conditions [3, 4]. As an appealing alternative, electrochemical nitrogen reduction reaction (eNRR) shows the potential for zero carbon emissions and operation under mild reaction conditions [5–7]. However, eNRR still suffers from sluggish kinetics and poor selectivity, primarily due to weak N_2 adsorption, the high energy barrier associated with N_2 activation, and the competing hydrogen evolution reaction (HER) [8–10].

Received: January 22, 2026; **Revised:** March 24, 2026
Accepted: April 9, 2026

✉Address correspondence to Shaobin Tang, tsb1980@xmu.edu.cn; Xin Xu, xxchem@fudan.edu.cn; Xijun Wang, xijun@ustc.edu.cn; Junjie Mao, maochem@ahnu.edu.cn

Transition metals (TM) single-atom catalysts (SACs) anchored on nitrogen-doped carbon materials (i.e., M-N_x-C) have emerged as promising eNRR catalysts [11–13]. Among these, M-N_3-C catalysts exhibit notable activity [14–21]. For example, Han et al. synthesized Mo-N_3-C embedded in N-doped porous carbon, achieving a high NH_3 yield of 34.0 ± 3.6 $\mu g \cdot h^{-1} \cdot mg_{cat.}^{-1}$ in alkaline medium [22]. However, the M-N_3-C sites suffer from low stability due to their highly unsaturated coordination structures. Recently, several experiment studies demonstrated the successful preparation of M-N_4-C configurations with improved stability for eNRR applications [23–26]. However, significant challenges remain: N_2 activation at M-N_4-C sites is insufficient, and overpotentials are still too high, limiting their eNRR efficiency [27, 28]. Very recently, the advanced eNRRCrew framework, a multi-agent framework that combines large language models (LLMs), machine learning, and automated tools, has been constructed to screen the promising eNRR catalysts [29]. Subsequently, the predicted bimetallic Fe-Mo catalyst by eNRRCrew framework is successfully prepared with impressive catalytic performance [30].

Two-dimensional layered molybdenum disulfide (MoS_2) is another promising electrocatalytic material, favorable for its superior electrical properties, low cost, and high stability [31–33]. In particular, introducing sulfur vacancy defects (V_s) on its basal plane (denoted as MoS_2-V_s) generates favorable active sites [34–36]. Our previous work showed that spin moments of the exposed Mo atoms at V_s sites, modulated by the TM dopants, significantly enhances N_2-to-NH_3 conversions [37]. Furthermore, a recent experimental study demonstrated that replacing the exposed Mo atom with Co modifies the electronic properties of V_s sites, lowers the energy barrier of the potential-determining step (PDS), and thus improves eNRR activity [38]. However, these modified MoS_2 materials still face limitations for poor conductivity and limited N_2 adsorption capacity, which greatly restrict their overall eNRR performance.

Recently, several studies have shown that spatial confinement effect plays a crucial role in enhancing the catalytic activity of SACs [39–43]. The density functional theory calculations by Huang et al. showed that by intercalating Sn into the interlayer space, the interlayer electrostatic repulsion in WS_2 bilayer is enhanced, and dynamic charge density fluctuations is suppressed [44]. The unique microenvironment provided by confined space not only enables isolated active site to modify the energy-scaling relationships, but also serves as nano-reactors that prevent contamination by foreign molecules. Therefore, we hypothesize that vertically stacking M-N_4-C with TM-doped MoS_2-V_s to form a M-N_4-C/MoS_2-TM bilayer could create an interlayer space with unique confinement effects, which might have the potential to synergistically modulate the intermediate adsorption and reaction so as to enhance eNRR performance.

Herein, using first-principles calculations, we investigated eNRR performance in the interlayer structures formed by Mn-N_4-C/MoS_2-TM bilayer with TM atoms doped on single V_s sites. Our results reveal that the interlayer space functions as a promising reaction platform, where the Mn-N_4-C site and the MoS_2-TM site act as dual sites, providing synergistic interactions with reaction intermediates. As a result, compared to the individual systems, the dual site hybrid systems significantly enhance N_2 adsorption and activation, while stabilizing the key intermediate $*N_2H$. Notably, active site switching between the MoS_2-TM and Mn-N_4-C sites during catalysis lowers the energy barrier of the PDS, i.e., $*NH_2 \rightarrow *NH_3$. Upon examining all 3d and 4d TM dopants, Mn-N_4-C/MoS_2-TM (TM = Mn, Tc, and Ag) have been identified as the most promising eNRR catalysts, exhibiting a low limiting potential of −0.3 V and a maximum kinetic barrier of 0.75 eV. In addition, based solely on intrinsic atomic properties (i.e., the number of d electrons (θ_d) and the electronegativity (X_{TM})) of the TM dopants, we developed an effective descriptor, $\varphi = \sqrt{\theta_d \times X_{TM}}$, that can accurately predict eNRR activity of the Mn-N_4-C/MoS_2-TM bilayer systems.

2 Computational methods

All calculations were carried out using the Vienna *ab initio* simulation package (VASP) [45] with the projector-augmented wave (PAW) [46] method to account for the electron–ion interactions. Spin-polarized calculations were adopted to describe the unpaired electrons of TM atoms. The exchange-correlation potential was treated by using the generalized gradient approximation (GGA) in the form of Perdew–Burke–Ernzerhof (PBE) functional [47]. A plane-wave basis set with a cut-off energy of 450 eV was used and long-range van der Waals interactions were corrected using the density functional theory (DFT)-D2 method proposed by Grimme [48]. The Brillouin zone was sampled with a 3 × 1 × 3 Monkhorst–Pack *k*-point mesh for geometry optimizations. The convergence criteria were set to 10^{-5} eV for energy and 0.02 eV/Å for forces on all atoms. A vacuum layer of 20 Å was added to eliminate interactions between periodic images. Atomic charges were calculated using Bader charge population analysis [49, 50]. Transition states (TS) for intermediate formation were searched using the climbing image nudged elastic band (CI-NEB) method [51].

The Mn-N_4-C/MoS_2-TM bilayer model was constructed by matching a 4 × 1 × 4 supercell of 2H-MoS_2 with a 5 × 1 × 5 supercell of pristine graphene, resulting in a lattice mismatch of less than 3%. The Mn-N_4-C configuration was formed by anchoring a single Mn atom on graphene, stabilized by four neighboring pyridine N atoms. The MoS_2-TM structures were constructed through two successive steps: First, an S atom was removed from the MoS_2 basal plane, creating a V_s site that exposes three undercoordinated Mo atoms; then, one of the exposed Mo atoms was substituted with a TM atom to form the MoS_2-TM structure. All 3d and 4d TM dopants were examined.

To evaluate the catalytic activity, the free energy change of each elementary step in eNRR was calculated using the computational hydrogen electrode (CHE) [52] model based on $\Delta G = \Delta E + \Delta E_{ZPE} - T\Delta S + \Delta G_U + \Delta G_{pH}$. Here, ΔE, ΔE_{ZPE}, and ΔS are the electronic energy difference between the initial and final states, the zero-point energy change, and the entropy change, respectively. $\Delta G_U = -eU$ accounts for the effect of the electrode potential *U*, while the temperature *T* was set to 298.15 K. The values of ΔE_{ZPE} and ΔS for adsorbates were obtained from vibrational frequency analysis [53], while those for gas-phase molecules were taken from the NIST-JANAF thermodynamical tables [54]. The effect of pH could be estimated using $\Delta G_{pH} = k_B T \times \ln 10 \times pH$, where k_B represents the Boltzmann constant. Here in this work, pH was set to 0. The limiting potential (U_L) was determined by $U_L = -\Delta G_{max}/e$, where ΔG_{max} is the maximum free energy change among all elementary steps, corresponding to that of PDS.

To simulate the realistic electrochemical condition, the *U* versus standard hydrogen electrode (SHE) is determined by tuning the system work function. The total energy-potential relationship was

acquired by varying the unit cell excess charge from −2.0 e^- to +2.0 e^- in 0.5 e^- steps. Implicit solvation was modeled using the VASPsol code, with a dielectric constant of 80 to simulate aqueous electrolyte, and the effective surface tension was set to 0 [55, 56]. A Debye length of 3.0 Å was used in the linearized Poisson–Boltzmann model to describe the compensating charge.

3 Results and discussion

3.1 Synergistic effect on adsorption and activation of N_2

Effective N_2 adsorption and activation are prerequisites for efficient eNRR. We first investigated how the interlayer space of the Mn-N_4-C/MoS_2-TM bilayer modulates N_2 adsorption. Figures 1(a)–1(c) show the optimized geometries of N_2 adsorbed on Mn-N_4-C, MoS_2-Mn, and their hybrid bilayer, respectively (see Figs. S1 and S2 in the Electronic Supplementary Material (ESM) for other Mn-N_4-C/MoS_2-TM systems). In individual systems, N_2 binds solely to the Mn atom in the Mn-N_4-C configuration (Fig. 1(a)), or to the V_s site with exposed Mo and doped Mn atom in MoS_2-Mn (Fig. 1(b)). In contrast, within the Mn-N_4-C/MoS_2-Mn interlayer space, N_2 adopts an end-on configuration stabilized simultaneously by both Mn-N_4-C and MoS_2-Mn sites (Fig. 1(c)), highlighting the synergistic effect of the dual sites.

Figures 1(d) and 1(e) compare the N_2 adsorption free energy and the corresponding N≡N bond lengths in different systems. Notably, for all considered TM atoms, N_2 adsorption in the Mn-N_4-C/MoS_2-TM bilayer is spontaneous with the adsorption free energy of $*N_2$ ($\Delta G(*N_2) < 0$ (blue line in Fig. 1(d)) and stronger than that on the individual catalysts (black and red lines in Fig. 1(d)), with more negative $\Delta G(*N_2)$ values indicating enhanced binding. Concomitantly, depending on the identity of the TM dopant, the interlayer interface in Mn-N_4-C/MoS_2-TM elongates the N≡N bond length to 1.20–1.26 Å (Fig. 1(e)), which is significantly longer than that observed in individual systems, indicating enhanced N_2 activation. This improvement in N_2 adsorption and activation shall be attributed to the synergistic effect of the Mn-N_4-C and MoS_2-TM dual sites within the hybrid bilayer.

3.2 Electronic origins of enhanced N_2 activation

To gain insight into the enhanced N_2 activation, we examined the electronic structures of adsorbed N_2 on various systems. Figures 2(a)–2(c) present the charge density differences of N_2 adsorbed on Mn-N_4-C, MoS_2-Mn, and the Mn-N_4-C/MoS_2-Mn bilayer, respectively. Compared to the individual catalysts, significantly more electrons are transferred to the adsorbed N_2 (0.85 e^- versus 0.33 e^- and 0.41 e^-) for the Mn-N_4-C/MoS_2-Mn bilayer, as summarized in Table S1 in the ESM (which also includes data for other TM dopants). This increased electron density is expected to populate the π^* antibonding orbitals of N_2, thereby weakening the N≡N triple bond and facilitating its activation.

The calculated partial density of states (PDOS) analysis, which focus on the overlap between p of N_2 and d orbitals of the metal active centers, along with the crystal orbital Hamilton population (COHP) analysis of the N≡N bond, further supports the enhanced N_2 activation, as illustrated in Figs. 2(d)–2(f). In the Mn-N_4-C/MoS_2-Mn interlayer space, a greater number of N_2 π^* antibonding orbitals are occupied by electrons from the metal d states compared to those in the individual catalysts, leading to stronger back-donation and greater N≡N bond weaking. Additionally, the more positive integrated COHP (ICOHP) values for the N≡N bond confirm the increased electron population in these antibonding orbitals of N_2 (see the right panels in Figs. 2(d)–2(f) and Fig. S3 in the ESM for other hybrid systems).

In accordance with the electron "donation-back-donation" mechanism, we present schematic illustrations comparing N_2 activation on individual catalysts (Fig. 2(g)) and on the hybrid Mn-N_4-C/MoS_2-TM bilayers (Fig. 2(h)). For the individual catalysts,

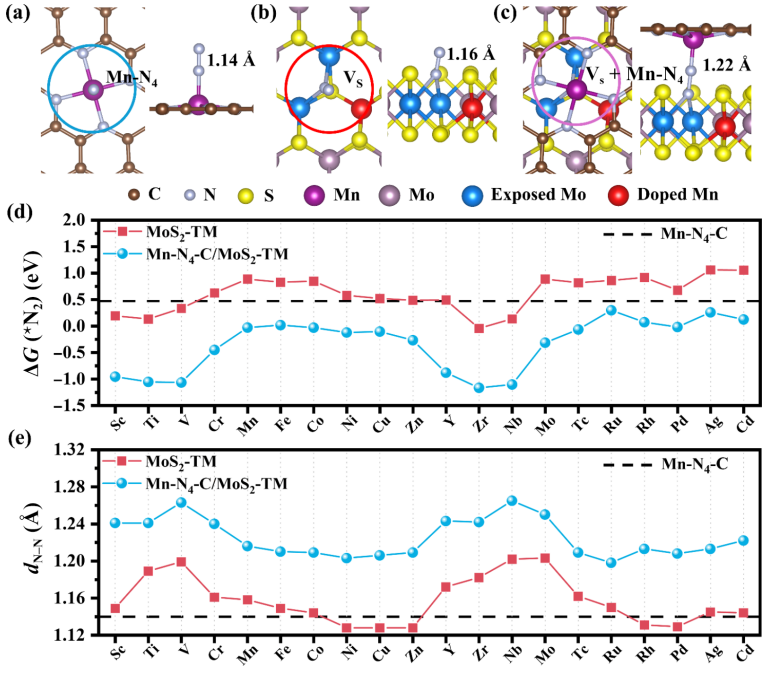

Figure 1 ((a)–(c)) Top and side views of geometrical structures for N_2 adsorbed on (a) Mn-N_4-C, (b) MoS_2-Mn, and (c) Mn-N_4-C/MoS_2-Mn. The circles indicate active sites, where the N≡N bond length is labelled. ((d) and (e)) Comparison of (d) N_2 adsorption free energies and (e) N≡N bond lengths in the Mn-N_4-C/MoS_2-TM bilayer system, as well as the individual systems.

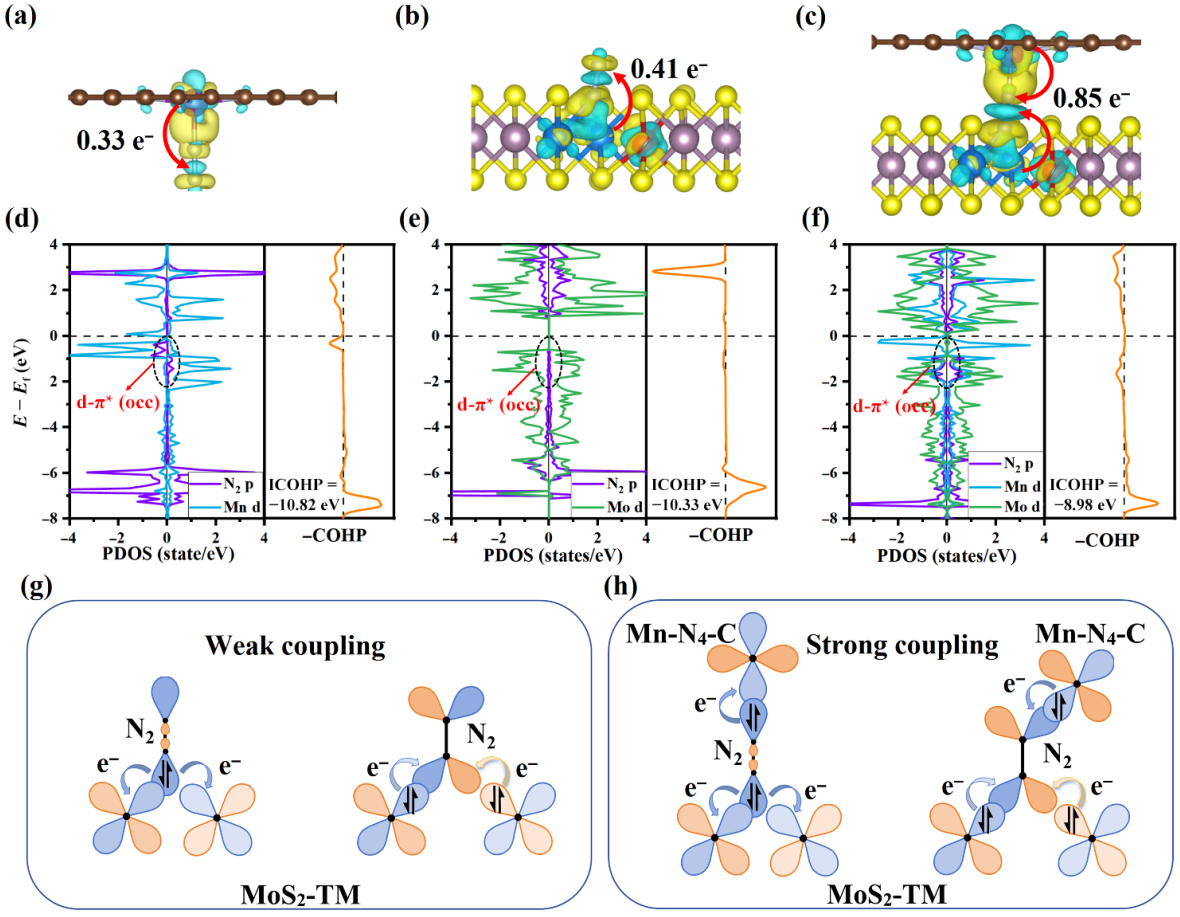

Figure 2 ((a)–(c)) Charge density differences and ((d)–(f)) spin polarized PDOS of the d orbitals of the metal active center and p orbitals of the adsorbed N_2 (left panel), along with the COHP (right panel of the N≡N bond, for N_2 adsorbed on ((a) and (d)) Mn-N_4-C, ((b) and (e)) MoS_2-Mn, and ((c) and (f)) Mn-N_4-C/MoS_2-Mn. In ((a)–(c)), the yellow and blue areas define electron accumulation and depletion, respectively, with an isosurface value of 0.005 e/Å^3, where the net electron transfer from catalysts to *N_2 is indicated. ((g) and (h)) Schematic comparison of electron "donation-back-donation" mechanism for N_2 adsorption and activation on MoS_2-TM (g) without and (h) with coupling to M-N_4-C.

only a single site, either Mn-N_4-C or MoS_2-TM, participates in the interactions between the metal d orbitals and the frontier molecular orbitals of N_2, leading to limited electron donation and back-donation, and thus weak N_2 adsorption and activation. In contrast, when Mn-N_4-C is vertically coupled with MoS_2-TM, the confined interlayer environment enables the d orbitals of both the Mn atom in Mn-N_4-C and the doped TM in MoS_2-TM to synergistically and directly interact with the frontier molecular orbitals of N_2, giving rise to stronger orbitals coupling from both π-back-donation (TM(d) → N_2π*) and σ-donation (TM(d) ← N_2σ).

3.3 Stabilization of the key intermediate *N_2H

It is widely accepted that an efficient eNRR catalyst should stabilize the adsorption of the *N_2H species to ensure effective N_2 activation [21, 57–59]. Figure 3(a) compares the adsorption free energies of *N_2H on isolated and hybrid systems. Clearly, the Mn-N_4-C/MoS_2-Mn bilayer exhibits a more negative adsorption free energy of *N_2H (ΔG(*N_2H)) than the individual MoS_2-Mn catalyst, indicating an enhanced *N_2H adsorption. To elucidate the mechanism behind this adsorption enhancement, we compared the geometries and electronic structures of *N_2H adsorbed on different catalysts.

On the individual MoS_2-Mn surface, only the proximal-N atom of *N_2H binds to the V_s site (Fig. 3(b1)). In contrast, within the interlayer space of Mn-N_4-C/MoS_2-Mn, both the proximal and distal N atoms of the *N_2H intermediate are selectively adsorbed, binding to the MoS_2-Mn site and the Mn-N_4-C site, respectively (Fig. 3(b2)). This dual site interaction highlights the synergetic effect, which significantly enhances the *N_2H adsorption. The calculated charge density differences show that the *N_2H intermediate accepts more electron density from the interlayer interface of the bilayer compared to the isolated catalyst (0.85 e^- vs. 0.55 e^-, see Figs. 3(b3) and 3(b4), and Table S2 in the ESM for other hybrid systems). Furthermore, comparison of the PDOS for *N_2H adsorbed on the isolated and hybrid systems (Figs. 3(b5) and 3(b6)) reveals that, within the energy window from −4 to −1 eV relative to the Fermi level, the synergistic interaction between the MoS_2-Mn site and the Mn-N_4-C site results in broader PDOS peaks for *N_2H, suggesting enhanced orbital overlap between *N_2H and the d orbitals of the metal center.

Figure 3(c) depicts a schematic illustration, comparing N_2 adsorption and activation on individual versus hybrid catalysts. Clearly, adsorption of the *N_2H intermediate, and more importantly N_2 itself, is significantly more favorable on the Mn-N_4-C/MoS_2-TM hybrid than on the individual components. The first hydrogenation step, converting *N_2 to *N_2H, is generally considered a key descriptor for assessing N_2 activation and overall catalytic activity [9, 60]. Our calculations show that the free energy barrier for *N_2 to *N_2H conversion (ΔG(*N_2 → *N_2H)) on Mn-N_4-C/MoS_2-

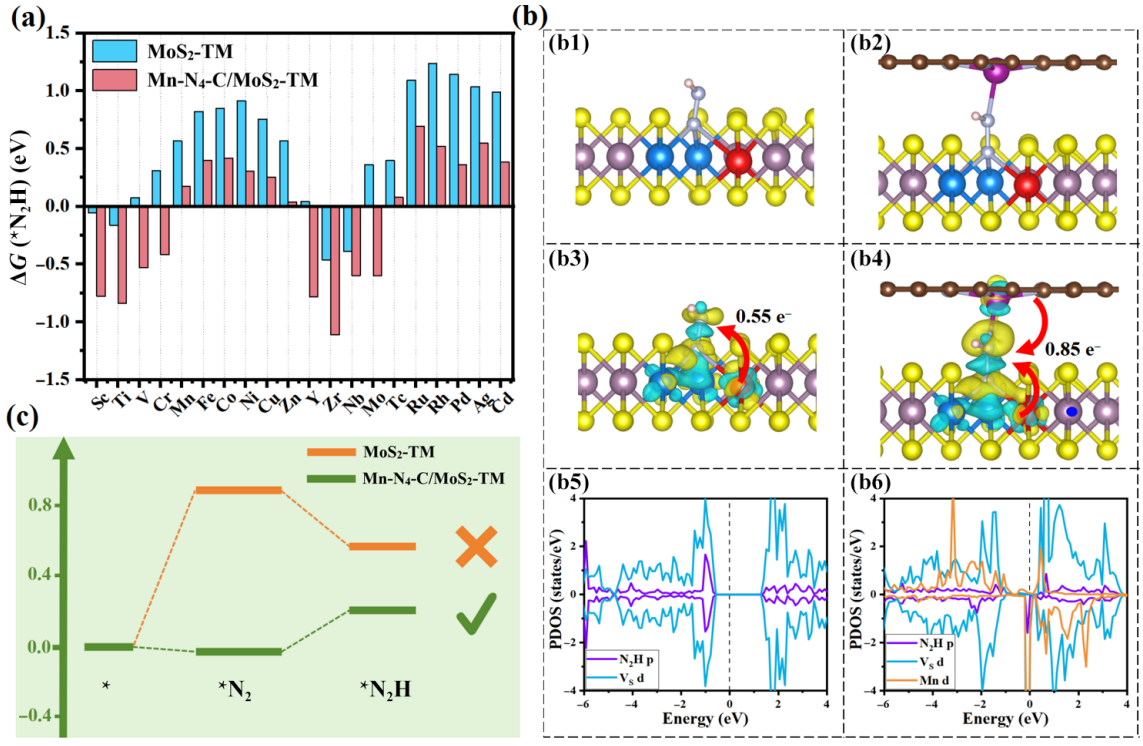

Figure 3 (a) Comparison of *N_2H adsorption free energy on MoS_2-TM and Mn-N_4-C/MoS2-TM. (b) ((b1) and (b2)) Geometrical structures, ((b3) and (b4)) charge density differences, and ((b5) and (b6)) spin polarized PDOS of the d orbitals of metal center and p orbitals of adsorbed *N_2H on ((b1), (b3), and (b5)) MoS_2-Mn and ((b2), (b4), and (b6)) Mn-N_4-C/MoS_2-Mn catalysts. The yellow and blue areas in (b3) and (b4) represent electron accumulation and electron depletion, respectively, with an isosurface value of 0.005 e/Å^3, where charge transfer from catalysts to *N_2H is indicated. (c) Schematic illustration comparing the energetics of N_2 adsorption and activation on the MoS_2-TM systems with and without coupling to Mn-N_4-C.

TM is slightly higher than that on the individual systems (see Fig. S4 in the ESM). However, the low ΔG(*N_2 → *N_2H) values observed for the individual catalysts are misleading: They arise from the highly unfavorable N_2 adsorption, which elevates the total energy of the reactant state (*N_2), and thereby artificially lows the corresponding reaction barrier. In contrast to previous studies that have interpreted low ΔG(*N_2 → *N_2H) values as indicators of strong N_2 activation while overlooking the detrimental effect of weak N_2 adsorption [61, 62], the present design of the hybrid bilayer system achieves genuine N_2 activation by enabling favorable adsorption of both *N_2 and *N_2H, providing a more reliable pathway for efficient eNRR.

3.4 Schematic reaction pathway for electrochemical N_2 reduction to NH_3

To evaluate the catalytic activity, we investigated the complete reaction pathway of eNRR. Figure 4 presents a schematic illustration of the plausible pathways occurring within the interlayer space of Mn-N_4-C/MoS_2-TM. For the formation of the first three intermediates, including *N_2, *N_2H, and *N-NH_2, both the MoS_2-TM and M-N_4-C sites are available as potential binding sites. Energetic analyses reveal that this dual site configuration enables more favorable binding of these intermediates compared to either individual site alone (see Figs. 1(d), 3(a), and Fig. S5 in the ESM for forming *N_2, *N_2H, and *N-NH_2, respectively). Consequently, the synergistic interaction between the MoS_2-TM and M-N_4-C sites plays a crucial role in facilitating the first two hydrogenation steps of the NRR process.

For the third hydrogenation step, which converts *N-NH_2 to *N-NH_3, two possible reaction pathways were examined, depending on whether the N–N bond is cleaved. In the first pathway, cleavage of the N–N bond leads to *N and *NH_3 intermediates, which adsorb on the MoS_2-TM site and the Mn-N_4-C site, respectively. In the second pathway, the *N-NH_3 species retains its N–N bond and remains adsorbed solely on the MoS_2-TM site. Total energy calculations show that the first pathway involving N–N bond dissociation is energetically more favorable than the one preserving the N–N bond (Fig. S6 in the ESM).

After desorption of the first NH_3 molecule, only one of the two binding sites participates in the adsorption of the remaining *NH_x species. Stating from the fourth hydrogenation step, three reaction pathways are possible, depending on the type of binding sites: MoS_2-TM, Mn-N_4-C, or a combination of both. In the mixed-site pathway, total energy calculations reveal that *NH and *NH_2 species preferentially adsorb on the MoS_2-TM site, while *NH_3 exhibits a strong preference to the Mn-N_4-C site (detailed energetics are provided in Table S3 in the ESM). This switching of the binding site from MoS_2-TM to Mn-N_4-C for *NH_3 helps lower the energy barrier for the critical *NH_2 to *NH_3 conversion step. Therefore, the mixed-site pathway is the most energetically favorable and is discussed in detail in the following sections.

3.5 The mixed-site reaction pathway and active site switching

Figure 5(a) presents the PDS and the corresponding Gibbs free energy change (ΔG_{PDS}) for N_2 reduction to NH_3 on the Mn-N_4-C/MoS_2-TM (TM = 3d and 4d) bilayer along the optimal pathway (see Table S4 in the ESM for details). For comparison, the ΔG_{PDS} values for the isolated Mn-N_4-C and MoS_2-TM catalysts are also shown. Depending on the identity of the TM dopant at the V_s site,

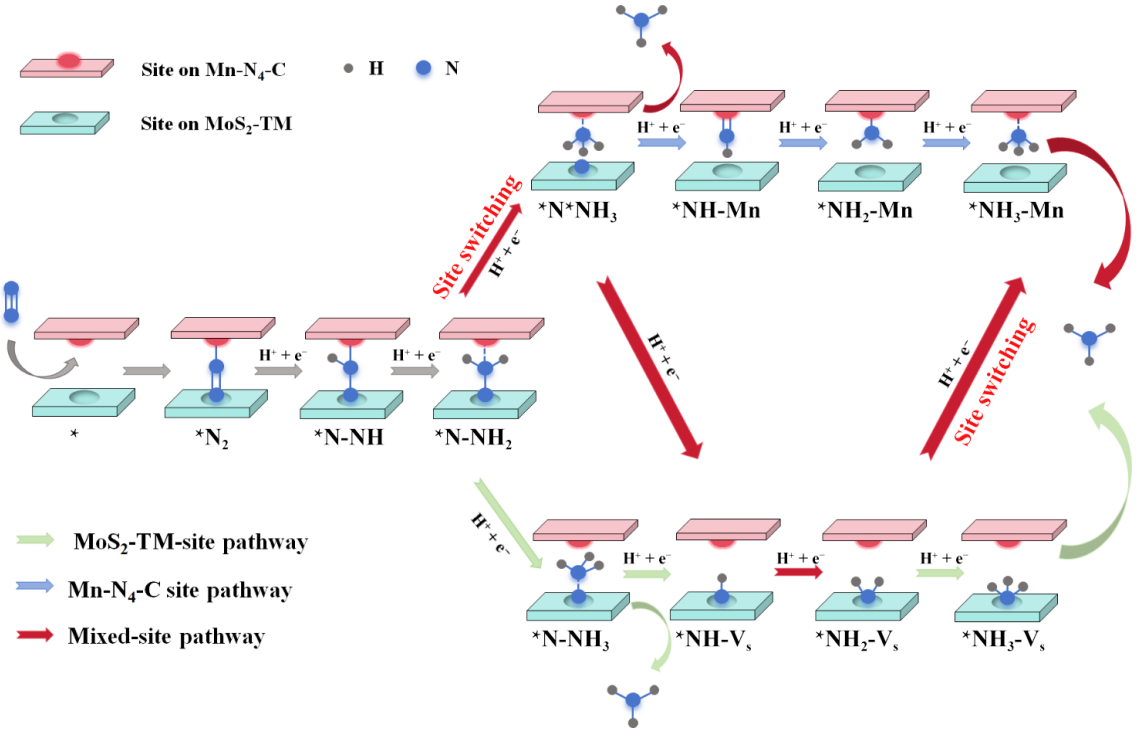

Figure 4 Schematic reaction pathway for electrochemical N_2 reduction to NH_3 occurred in the interlayer space of Mn-N_4-C/MoS_2-TM.

one of four elementary steps is identified as the PDS: (1) $*N_2 + H^+ + e^- \rightarrow *N_2H$, (2) $*N - NH_2 + H^+ + e^- \rightarrow *N - NH_3$, (3) $*NH + H^+ + e^- \rightarrow *NH_2$, and (4) $*NH_2 + H^+ + e^- \rightarrow *NH_3$. Clearly, compared to the individual catalysts, coupling Mn-N_4-C with MoS_2-TM significantly lowers the ΔG_{PDS}, indicating improved catalytic activity. In particular, three hybrid catalysts, Mn-N_4-C/MoS_2-TM with TM = Mn, Tc, and Ag, exhibit outstanding eNRR catalytic activity, with ΔG_{PDS} values below 0.3 eV.

To gain deeper insight into the effect of coupling the MoS_2-TM and Mn-N_4-C sites on the eNRR reaction pathway, we compared the Gibbs free energy diagrams for the promising Mn-N_4-C/MoS_2-TM systems (TM = Mn and Tc) with those of their individual components, as illustrated in Figs. 5(b) and 5(c) (see Figs. S7 and S8 in the ESM for other TM dopants). The coupling of the MoS_2-TM with the Mn-N_4-C site leads to distinct changes in catalytic behavior. For the isolated systems, Mn-N_4-C has a PDS of $*N_2 + H^+ + e^- \rightarrow *N_2H$, while MoS_2-TM (TM = Mn and Tc) has a PDS of $*NH_2 + H^+ + e^- \rightarrow *NH_3$, respectively. The hybrid Mn-N_4-C/MoS_2-Mn system retains the same PDS as does the isolated MoS_2-Mn. In contrast, when coupled with MoS_2-Tc, the hybrid bilayer system alters its PDS to $*NH + H^+ + e^- \rightarrow *NH_2$. This change results in a significantly reduced ΔG_{PDS} of approximately 0.3 eV, compared to 0.62 eV for the respective MoS_2-Tc catalyst.

Figure 5(d) compares the geometrical structures of eNRR intermediates on the isolated and hybrid systems. It is evident that the coupling of the MoS_2-TM and Mn-N_4-C sites alters the adsorption behavior of the intermediates confined in interlayer space of Mn-N_4-C/MoS_2-TM. In particular, switching the active site from MoS_2-TM to Mn-N_4-C during the $*NH_2$ to $*NH_3$ conversion is readily achieved, requiring only to overcome a small migration barrier of 0.24 eV (Fig. S9 in the ESM), and thereby lowering the ΔG_{PDS}. This synergistic effect between the MoS_2-TM and Mn-N_4-C sites within the interlayer space is also observed in Fe-N_4-C/MoS_2-TM systems (Figs. S10–S13 in the ESM).

As shown in Fig. S14 in the ESM, the adsorbed $*N*NH_3$ leads to larger interlayer distance (3.67 Å) compared to other intermediates (3.31–3.52 Å). Thus, effect of the interlayer distance on the overall catalytic performance is investigated. The N_2 adsorption is significantly weakened with increasing interlayer distance, whereas the key steps $*N_2 + H^+ + e^- \rightarrow *N_2H$ and $*NH_2 + H^+ + e^- \rightarrow *NH_3$ become more favorable (Fig. S15 and Table S5 in the ESM). In addition, we also considered the solvent effect on the reaction pathway and the binding stability of intermediates. The calculated results showed that the explicit water environment still maintains the more favorable site switching pathway, and also has a small influence on the corresponding ΔG_{PDS} (see Figs. S16–S18 in the ESM for detail).

The active site configuration and synergistic interaction mechanism in designed Mn-N_4-C/Mo_2-TM bilayer are distinct different from that in previous reported works including the vertical heterostructures [63–65], TM-doped S vacancies [66, 67], and dual-metal atoms anchored on N-doped carbon [68] (see Table S6 in the ESM for details). For example, in $MoS_2/NiPS_3$ vertical heterostructure, the hydrogen spillover and deprotonation are synergistically proceeded at $NiPS_3$ and MoS_2 regions by the internal polarization field, respectively, realizing efficient water electrolysis. Previous interaction mechanisms only highlighted the synergetic adsorption of intermediates between dual sites associated with the regulation of electronic structure of active site by the adjacent metal atom, while these mechanisms have neglected the spatial effect. The combination of space confinement and synergistic effect in the Mn-N_4-C/Mo_2-TM bilayer could offer more possibilities for optimizing reaction pathways.

3.6 Electronic origins of catalytic activity modulated by the TM dopant

To elucidate the electronic origins of catalytic activity modulated by TM atom doping, we investigated the charge redistribution of the

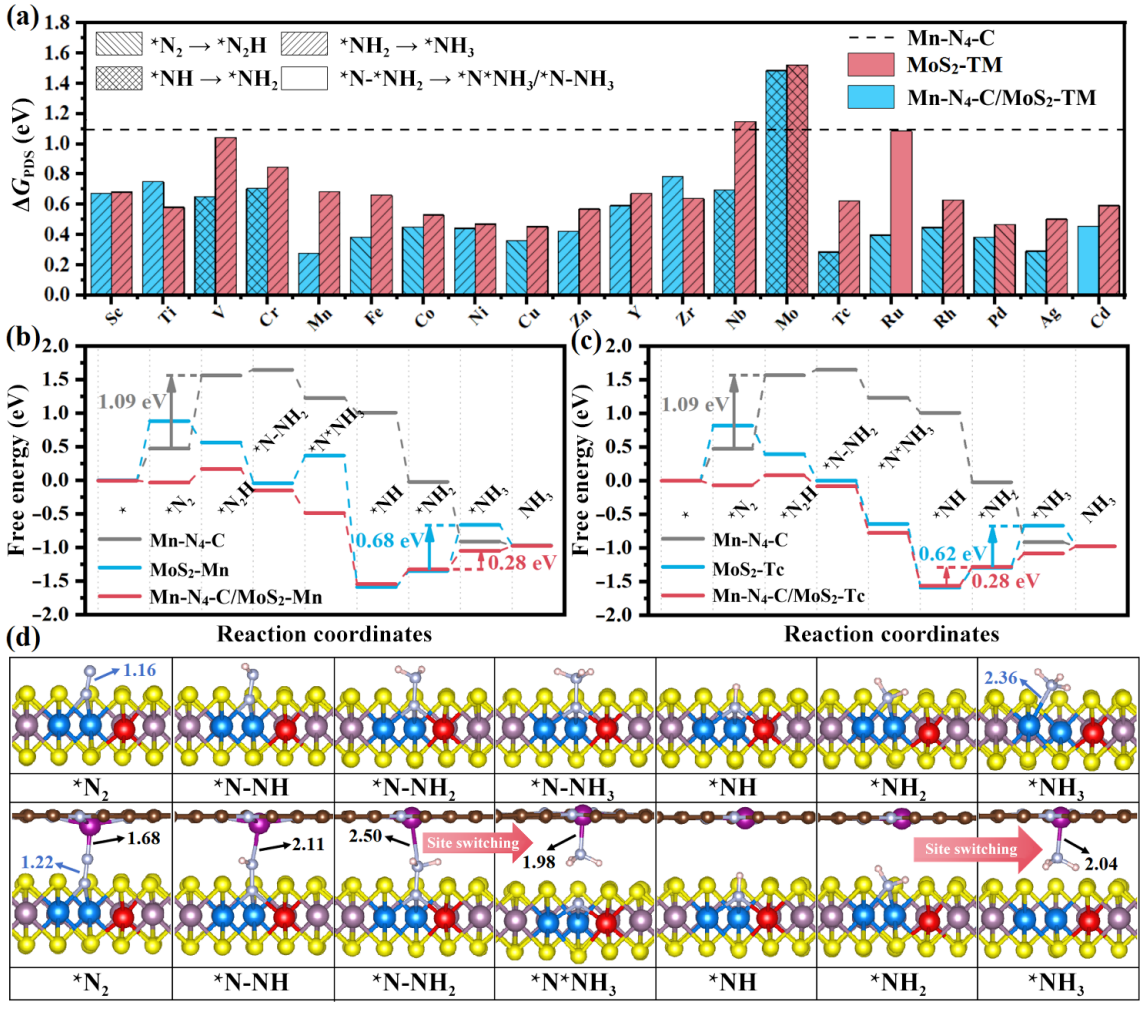

Figure 5 ((a)–(c)) Comparison of (a) ΔG_{PDS} of the potential-determining step and ((b) and (c)) free energy diagrams for N_2 reduction to NH_3 via the mixed-site pathway on Mn-N_4-C, MoS_2-TM, and Mn-N_4-C/MoS_2-TM. In (b) and (c), TM = Mn and Tc atoms, respectively, and the vertical arrows define the ΔG_{PDS}. (d) Comparison of geometry structures (distance in Å) of eNRR intermediates adsorbed on MoS_2-Mn and Mn-N_4-C/MoS_2-M.

exposed Mo and the TM dopants, as well as their correlations with intermediate binding. Charge density difference calculations reveal that, compared to the pristine V_s site (Fig. 6(a)), TM dopants alter the polarized charge distribution on the exposed Mo atoms (Figs. 6(b) and 6(c)). In particular, doping with Mn or Tc enhances the charge polarization of the exposed Mo atoms, with electrons transfers of 1.89 e^- or 1.87 e^-, respectively, compared to 1.85 e^- for the undoped case. To better describe the effect of dopant TM atom on the electronic structure of exposed Mo atoms, the polarized charges of TM and Mo atoms (denoted as ΔQ_{Mo} and ΔQ_{TM}, respectively) were calculated by the Bader charge of the S-vacancy Mo atoms and the doped TM atoms in Mn-N_4-C/MoS_2-TM minus the valence electron number of free Mo and TM atoms, respectively.

An approximately linear scaling relationship between ΔQ_{Mo} and ΔQ_{TM} suggests that the doped TM atoms regulate the charge distribution of exposed Mo active center (Fig. 6(d)). The TM dopants located towards the right side of the periodic table (such as Pd, Ru, Ag, and Cd) tend to accept more electrons from the Mo atoms, thereby enhancing Mo charge polarization (corresponding to a reduction in Mo electron density). An inverse linear relationship between ΔQ_{Mo} and the adsorption free energy (ΔG) of intermediates suggests that a TM dopant with decreased $|\Delta Q_{TM}|$ weakens the adsorption of intermediates such as $*N_2$, $*N_2H$, *NH, and $*NH_2$ (Figs. 6(e) and 6(f)). This modulation of intermediate binding strength plays a crucial role in regulating eNRR catalytic activity.

3.7 Rational design of Mn-N_4-C/MoS_2-TM catalysts for eNRR

Developing an effective descriptor is crucial for predicting catalytic activity and screening promising catalytic materials [69]. Previous studies showed that the adsorption free energy of key intermediates, such as $*N_2H$ ($\Delta G(*N_2H)$), can serve as an indicator of catalytic activity [58, 70, 71]. Herein, we investigated the relationship between $\Delta G(*N_2H)$ and the binding energies of $*N_2$, *NH, and $*NH_2$, as shown in Figs. 7(a)–7(c) (see Fig. S19 in the ESM for other species). High correlation coefficients ($R^2 > 0.82$) indicate a strong linear relationship between the binding strength of $*N_2H$ and the overall catalytic process of eNRR. In general, the designed hybrid Mn-N_4-C/MoS_2-TM materials with weak $*N_2H$ adsorption, such as those doped with Tc, Mn, Ag, and Ru, exhibit superior catalytic activity, as evidenced by their low ΔG_{PDS} values (Fig. 7(d)).

For rational design of single-atom electrocatalysts, developing a practical descriptor based solely on intrinsic material properties is

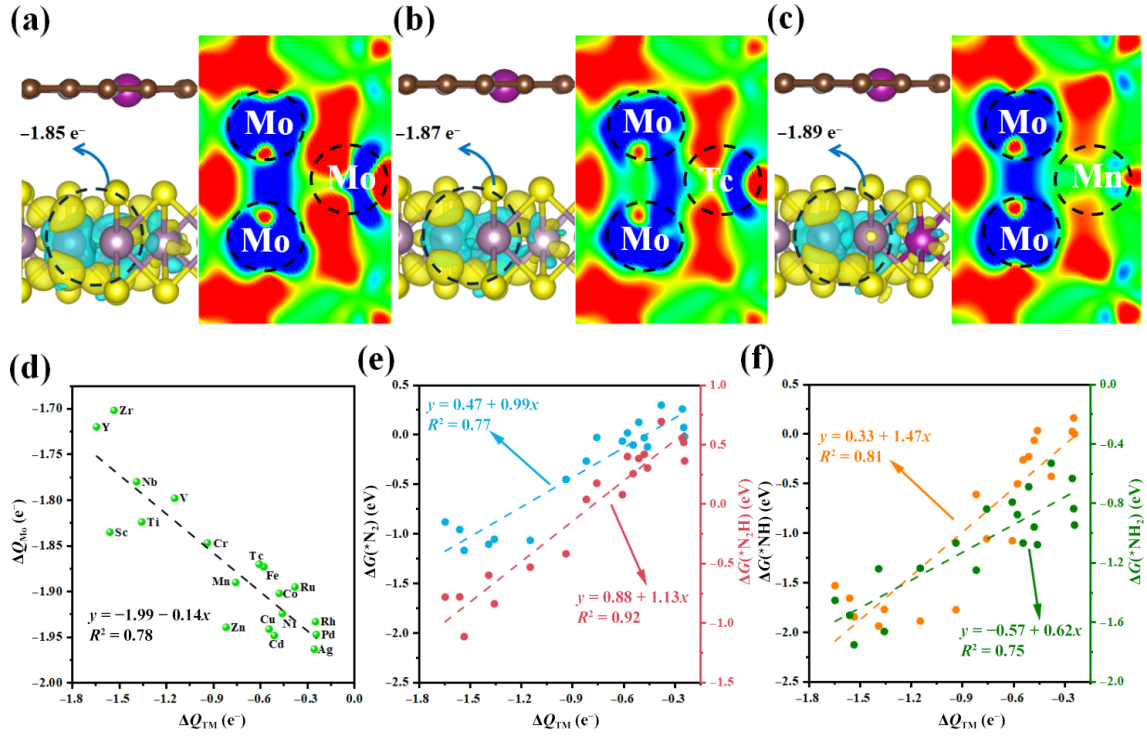

Figure 6 ((a)–(c)) Polarized charge distribution on the exposed Mo atoms in the Mn-N_4-C/MoS_2-TM bilayer with (a) doped TM = Mo, (b) Tc, and (c) Mn. ((d)–(f)) Correlation between the polarized charges of the TM dopants (ΔQ_{TM}) with (d) the polarized charges of two exposed Mo atoms (ΔQ_{Mo}), (e) ΔG(*N_2) and ΔG(*N_2H), and (f) the adsorption free energy of *NH (ΔG(*NH)) and *NH_2 (ΔG(*NH_2)). The isosurface values in ((a)–(c)) are set to 0.008 e/Å^3.

highly desired. Inspired by previous studies [72, 73], two intrinsic atomic properties of the TM dopants, d electrons (θ_d) and electronegativity (X_{TM}), which are highly related to charge transfer, are selected to establish a quantitative structure–property relationship. A series of descriptors consisting of the θ_d and X_{TM} and their various combination are constructed (Table S7 in the ESM). By comparing the correlation between these descriptors and ΔG(*N_2H) and ΔQ_{TM}, a simple mathematic expression (φ), defined as ($\varphi = \sqrt{\theta_d \times X_{TM}}$), is determined to be an excellent descriptor due to the high correlation coefficients (R^2 = 0.87 and 0.80 in Figs. 7(e) and 7(f), respectively), compared to other expressions (Table S7 in the ESM). Therefore, the descriptor, relying solely on intrinsic material properties, accurately captures the electronic structure of the metal active sites and their interaction with reaction intermediates.

This effective descriptor enables rapid and precise screening of eNRR electrocatalysts by selecting appropriate TM dopants in Mn-N_4-C/MoS_2-TM materials. By considering the dataset of 5d metals, we used the φ to predict the ΔG_{PDS}. As a result, the Au is screened out as promising dopant for NRR due to the lowest ΔG_{PDS} (Figs. S20 and S21 in the ESM). Different from the previous reported descriptors that depend on the coordination environments and even on the DFT calculated values [74, 75], the descriptor φ solely relies on the intrinsic poetries of metal center.

3.8 Kinetics for NRR on the Mn-N_4-C/MoS_2-Mn bilayer catalyst

In addition to the favorable thermodynamics discussed above, kinetic behavior is also an essential factor governing eNRR activity. Here, we investigated the kinetic barriers for NRR on the Mn-N_4-C/MoS_2-Mn catalyst using the method proposed by Janik et al. [76]. The full reaction energy profile and the corresponding geometries of intermediates and TS are presented in Fig. 8. To facilitate the hydrogenation of intermediates, the incoming H atom can be adsorbed either on the N site in the M-N_4-C component or on the S atom adjacent to the V_s site, depending on the interaction pattern of each intermediate. Hydrogenation at the N site enables elementary steps such as *N-N to *N-NH, *N-NH_2 to *N*NH_3, and *NH_2 to *NH_3 species, while hydrogenation at the S site promotes elementary steps of *N-NH to *N-NH_2 and *NH to *NH_2 (Fig. 8(b)). A comparison of the minimum energy pathways for different H sites showed that the H weak adsorption at initial site leads to a lower barrier for hydrogenation of intermediates, compared to the H strong adsorption (see Fig. S22 in the ESM for detail).

Among all elementary steps, the final hydrogenation of *NH_2 to form *NH_3 on the MoS_2-Mn site exhibits the highest activation barrier of 0.75 eV, making it the kinetic rate-determining step (RDS). The hydrogenation of *N-NH to *N-NH_2 has the second highest barrier of 0.58 eV, while all other steps proceed readily with activation barriers below 0.5 eV. Notably, after the final hydrogenation step, *NH_3 desorption is facilitated by a favorable site-switching from the MoS_2-Mn site to the Mn-N_4-C site, requiring only a minor migration barrier of 0.24 eV. The predicted maximum activation barrier is significantly lower than that on the Ru(0001) surface (1.08 eV) [77], indicating excellent kinetics for N_2 reduction to NH_3 on the designed Mn-N_4-C/MoS_2-Mn bilayer catalyst.

3.9 HER competition and stability of Mn-N_4-C/MoS_2-TM catalyst

To develop excellent eNRR electrocatalysts, one also needs to compare the N_2 reduction with the competing HER. The catalytic selectivity of NRR is evaluated by the limiting potentials difference

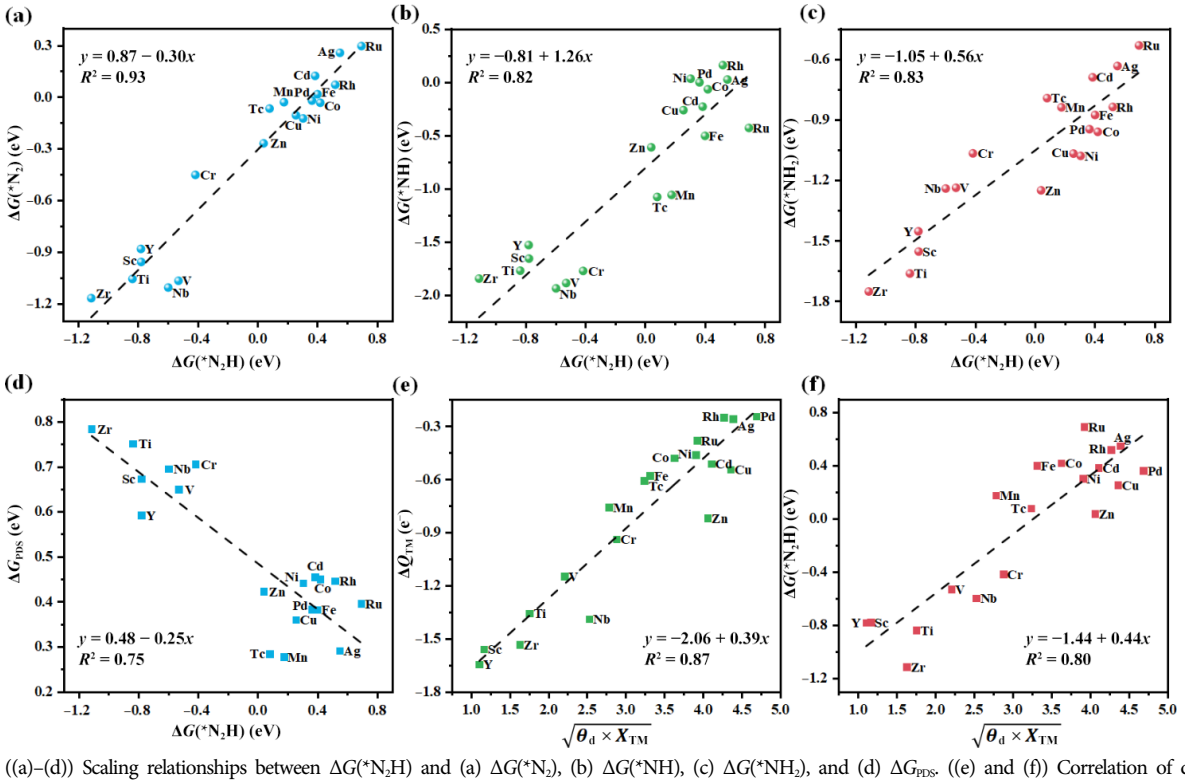

Figure 7 ((a)–(d)) Scaling relationships between $\Delta G(^*N_2H)$ and (a) $\Delta G(^*N_2)$, (b) $\Delta G(^*NH)$, (c) $\Delta G(^*NH_2)$, and (d) ΔG_{PDS}. ((e) and (f)) Correlation of descriptor $\varphi = \sqrt{\theta_d \times X_{TM}}$ with (e) ΔQ_{TM} and (f) $\Delta G(^*N_2H)$.

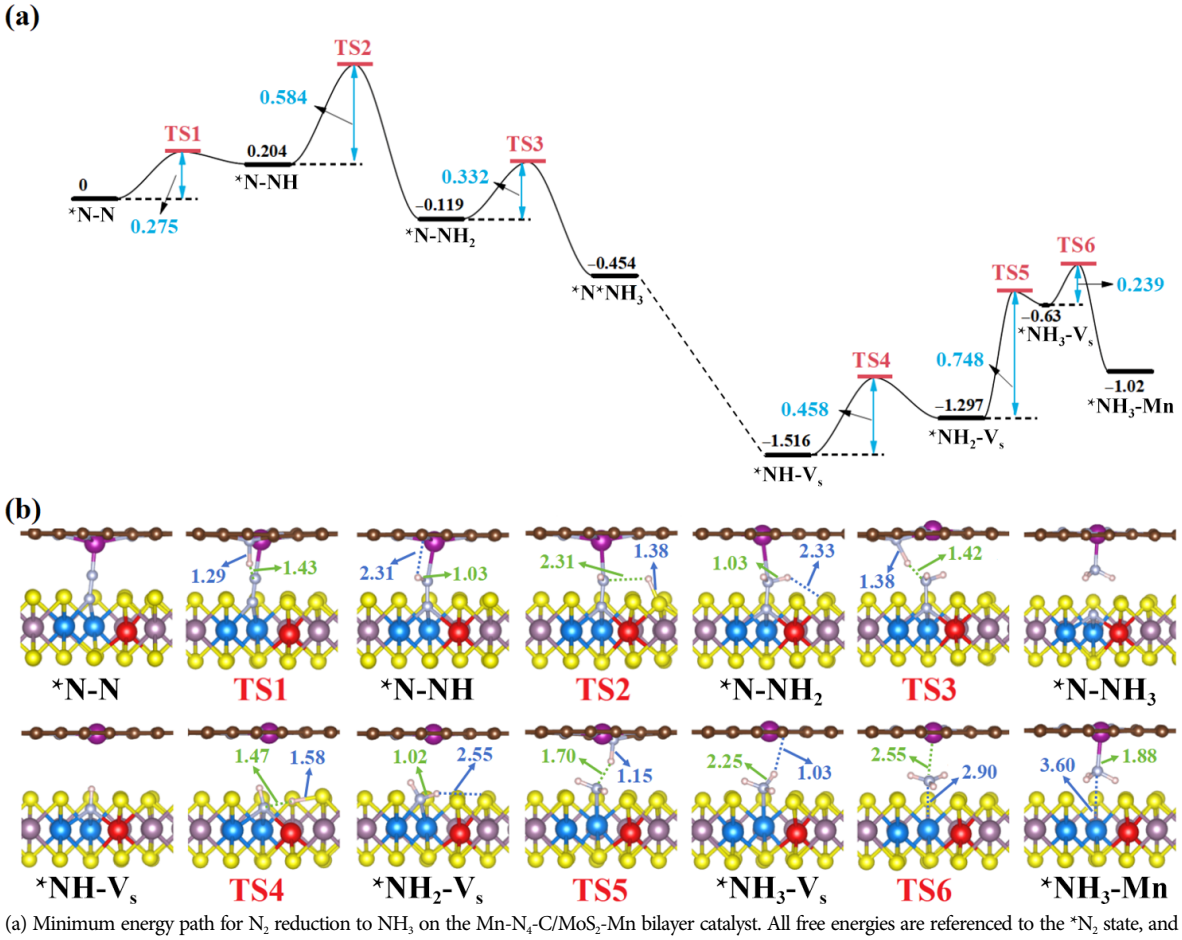

Figure 8 (a) Minimum energy path for N_2 reduction to NH_3 on the Mn-N_4-C/MoS_2-Mn bilayer catalyst. All free energies are referenced to the $^*N_2$ state, and activation barriers are marked with arrows. (b) Optimized structures of intermediates and TS, corresponding to those in (a). For simplicity, Mn is used to label the Mn-N_4-C site, while V_s is used to label the MoS_2-Mn site.

between NRR and HER ((U_L(NRR) − U_L(HER)) (Fig. 9(a)). All bilayer catalysts located above the red dashed line, which corresponds to the metal benchmark with a value of U_L(NRR) − U_L(HER) = 0.5 V, indicating optimum selectivity toward NRR [78]. In particular, the Mn, Tc, and Ag doped catalysts that possess high catalytic activity hold outstanding NRR sensitivity because their U_L(NRR) − U_L(HER) are close to zero. Furthermore, a comparison of kinetic activation barriers (Fig. 8(a) vs. Fig. 9(b)) shows that most of intermediate formations for NRR are more favorable than the coupling of two *H to form H_2, dynamically. The rating-determined step for *NH_2 to *NH_3 is comparable to H_2 generation (0.75 vs. 0.63 eV).

Then, we evaluated the stability of Mn-N_4-C/MoS_2-TM bilayer under electrochemical conditions. To this end, the coupling energy (E_c) of Mn-N_4-C and MoS_2-TM, formation energy of doped TM atom (E_f), and the dissolution potential (U_{diss}) of TM atoms are computed (see Fig. S23 and Table S8 in the ESM for computational details). The calculated results show that the formation of Mn-N_4-C/MoS_2-TM bilayer is thermodynamically favorable by coupling the corresponding isolated monolayer due to the negative E_c. Applying the less negative external potential (U) can improve the stability of the coupled bilayer catalysts (Fig. S24 in the ESM). All doped TM atoms with negative E_f exhibit higher stability compared to the corresponding bulk phase, indicating difficult aggregation into cluster (Table S8 in the ESM). Compared to the intrinsic Mo doping, the first transition metal atoms (Sc, Ti, V, Zr, and Nb) are more easily doped into the S vacancy due to more negative E_f. Dissolution of most of doped TM atoms is unlikely to occur due to the positive U_{diss}. Furthermore, the *ab initio* molecular dynamics (AIMD) simulations (Fig. S25 in the ESM) showed that the local atomic structures of Mn-N_4 and TM-doped S vacancy active centers remain unchanged at 1000 K after 4 ps, with only small distortion observed.

Previously, extensive experimental studies have reported the successful preparation of metal atom-doped MoS_2 and atomically dispersed single TM atom supported on carbon materials. For example, using the high-temperature pyrolysis and thermal activation of precursors, Lin et al. reported a facile strategy of crafting wrinkled MoS_2/N-doped carbon core/shell nanospheres interfaced with single Fe atoms (namely MoS_2@Fe-N-C) [79]. The Co-doped MoS_{2-x} polycrystalline nanosheets with sulfur vacancies were synthesized via a hydrothermal growth process using cobalt nitrate and thiourea precursors, followed by rapid cooling to induce defect formation [38]. Therefore, the coupled Mn-N_4-C/MoS_2-TM bilayer materials with controlled dopants and vacancies are expected to be experimentally realized through the synthetic routes as listed above.

4 Conclusions

In summary, using first-principles calculations, we systematically investigated the eNRR catalytic behavior within the interlayer space of the Mn-N_4-C/MoS_2-TM bilayer. Our results reveal that the MoS_2-TM/Mn-N_4-C moieties confined in the interlayer space serve as dual active sites. Their synergistic interaction optimizes the electron donation and back-donation between the d orbitals of the metal centers and the frontier molecular orbitals of N_2, thereby effectively regulating the adsorption behavior of reaction intermediates. Compared to individual single-component sites, the coupling of the MoS_2-TM and Mn-N_4-C sites greatly improves *N_2 and *N_2H adsorption, facilitates electron transfer from the metal centers to N_2, and elongates the N≡N bond length, leading to superior N_2 activation.

In particular, the switch of binding sites between MoS_2-TM and Mn-N_4-C for intermediate adsorption significantly optimizes the catalytic reaction pathway and lowers the free energy barrier of the potential-determining step. Detailed energetics and mechanistic analyses demonstrate that Mn-N_4-C/MoS_2-TM systems with TM = Mn, Tc, and Ag exhibit superior eNRR catalytic activity, with a low limiting potential of −0.3 V and a maximum activation barrier of 0.75 eV. Additionally, by relying solely on the θ_d and X_{TM} of the TM dopants, we revealed a novel descriptor $\varphi = \sqrt{\theta_d \times X_{TM}}$ to accurately predict the adsorption energy of key intermediates. These dual atom sites confined within interlayer interfaces of MoS_2-TM/Mn-N_4-C offer a promising design strategy for efficient electrochemical catalyst capable of mediating complex and multi-intermediate reactions such as eNRR.

Electronic Supplementary Material: Supplementary material (geometry and electronic structures and ICOHP of N≡N bond for the adsorbed N_2, comparison of charge transfer and adsorption energy of intermediates, interlayer distance effect, Gibbs free energy changes of elementary step, free energy diagrams on Mn-N_4-C/MoS_2-TM-related systems and other hybrid systems, correlation of adsorption free energy of intermediates, the predicted ΔG_{PDS} results, solvent effect, stability of catalysts, comparison with

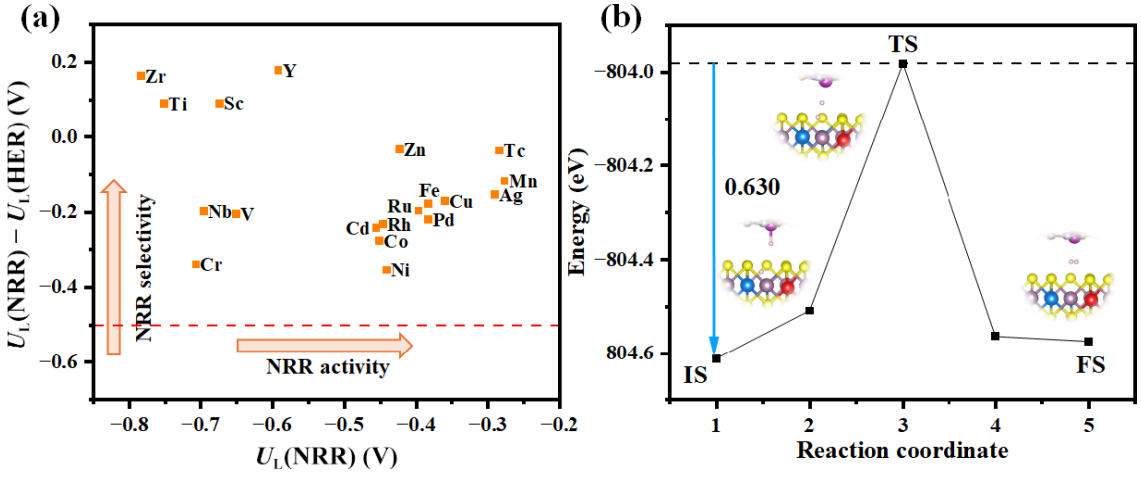

Figure 9 (a) Limiting potential of U_L(NRR) versus U_L(NRR) − U_L(HER). (b) Reaction energy profiles for coupling of two *H to form H_2 on Mn-N_4-C/MoS_2-Mn.

previous work, and AIMD simulation) is available in the online version of this article at https://doi.org/10.26599/NR.2026.94908724.

Data availability

All data needed to support the conclusions in the paper are presented in the manuscript and the Electronic Supplementary Material. Additional data related to this paper may be requested from the corresponding author upon request.

Acknowledgements

This work was financially supported by the National Natural Science Foundation of China (NSFC) (No. 22063001) and Jiangxi Provincial Natural Science Foundation (No. 20244BAB28057). The numerical calculations were done on the supercomputing system in the Supercomputing Center of University of Science and Technology of China.

Declaration of competing interest

All the contributing authors report no conflict of interests in this work.

Author contribution statement

G. P. W: Writing – original draft, software, investigation, data curation. Z. Z. J: Validation, investigation, formal analysis. X. J. W: Writing – original draft. T. T. H: Visualization, software. L. L. L: Software, data curation. Z. C. M: Visualization, software. L. Z: Methodology, data curation. J. J. M: Writing – review & editing. X. X: Writing – review & editing. S. B. T: Conceptualization, writing – review & editing, resources, project administration, funding acquisition. All the authors have approved the final manuscript.

Use of AI statement

None.

References

[1] Schlögl, R. Catalytic synthesis of ammonia—A "never-ending story". *Angew. Chem., Int. Ed.* **2003**, *42*, 2004–2008.

[2] Chen, J. G.; Crooks, R. M.; Seefeldt, L. C.; Bren, K. L.; Bullock, R. M.; Darensbourg, M. Y.; Holland, P. L.; Hoffman, B.; Janik, M. J.; Jones, A. K. et al. Beyond fossil fuel-driven nitrogen transformations. *Science* **2018**, *360*, eaar6611.

[3] Han, G. F.; Li, F.; Chen, Z. W.; Coppex, C.; Kim, S. J.; Noh, H. J.; Fu, Z. P.; Lu, Y. L.; Singh, C. V.; Siahrostami, S. et al. Mechanochemistry for ammonia synthesis under mild conditions. *Nat. Nanotechnol.* **2021**, *16*, 325–330.

[4] Kandemir, T.; Schuster, M. E.; Senyshyn, A.; Behrens, M.; Schlögl, R. The Haber–Bosch process revisited: On the real structure and stability of "ammonia iron" under working conditions. *Angew. Chem., Int. Ed.* **2013**, *52*, 12723–12726.

[5] Chanda, D.; Xing, R. M.; Xu, T.; Liu, Q.; Luo, Y. L.; Liu, S. H.; Tufa, R. A.; Dolla, T. H.; Montini, T.; Sun, X. P. Electrochemical nitrogen reduction: Recent progress and prospects. *Chem. Commun.* **2021**, *57*, 7335–7349.

[6] Yang, X.; Nash, J.; Anibal, J.; Dunwell, M.; Kattel, S.; Stavitski, E.; Attenkofer, K.; Chen, J. G.; Yan, Y. S.; Xu, B. J. Mechanistic insights into electrochemical nitrogen reduction reaction on vanadium nitride nanoparticles. *J. Am. Chem. Soc.* **2018**, *140*, 13387–13391.

[7] Zhang, L. L.; Ding, L. X.; Chen, G. F.; Yang, X. F.; Wang, H. H. Ammonia synthesis under ambient conditions: Selective electroreduction of dinitrogen to ammonia on black phosphorus nanosheets. *Angew. Chem., Int. Ed.* **2019**, *58*, 2612–2616.

[8] Han, L. L.; Ren, Z. H.; Ou, P. F.; Cheng, H.; Rui, N.; Lin, L. L.; Liu, X. J.; Zhuo, L. C.; Song, J.; Sun, J. Q. et al. Modulating single-atom palladium sites with copper for enhanced ambient ammonia electrosynthesis. *Angew. Chem., Int. Ed.* **2021**, *60*, 345–350.

[9] Singh, A. R.; Rohr, B. A.; Schwalbe, J. A.; Cargnello, M.; Chan, K.; Jaramillo, T. F.; Chorkendorff, I.; Nørskov, J. K. Electrochemical ammonia synthesis—The selectivity challenge. *ACS Catal.* **2017**, *7*, 706–709.

[10] Suryanto, B. H. R.; Du, H. L.; Wang, D. B.; Chen, J.; Simonov, A. N.; MacFarlane, D. R. Challenges and prospects in the catalysis of electroreduction of nitrogen to ammonia. *Nat. Catal.* **2019**, *2*, 290–296.

[11] Wen, Z. L.; Lv, H. F.; Wu, X. J. Single-atom low-valent alkaline-earth-metal catalysts for electrochemical nitrogen reduction with an acceptance-backdonation mechanism. *ACS Appl. Mater. Interfaces* **2022**, *14*, 52079–52086.

[12] Geng, Z. G.; Liu, Y.; Kong, X. D.; Li, P.; Li, K.; Liu, Z. Y.; Du, J. J.; Shu, M.; Si, R.; Zeng, J. Achieving a record-high yield rate of 120.9 $\mu g_{NH_3} \cdot mg_{cat}^{-1} \cdot h^{-1}$ for N_2 electrochemical reduction over Ru single-atom catalysts. *Adv. Mater.* **2018**, *30*, 1803498.

[13] Gu, Y.; Xi, B. J.; Tian, W. Z.; Zhang, H.; Fu, Q.; Xiong, S. L. Boosting selective nitrogen reduction via geometric coordination engineering on single-tungsten-atom catalysts. *Adv. Mater.* **2021**, *33*, 2100429.

[14] Wang, X. Q.; Wang, W. Y.; Qiao, M.; Wu, G.; Chen, W. X.; Yuan, T. W.; Xu, Q.; Chen, M.; Zhang, Y.; Wang, X. et al. Atomically dispersed Au_1 catalyst towards efficient electrochemical synthesis of ammonia. *Sci. Bull.* **2018**, *63*, 1246–1253.

[15] Mukherjee, S.; Yang, X. X.; Shan, W. T.; Samarakoon, W.; Karakalos, S.; Cullen, D. A.; More, K.; Wang, M. Y.; Feng, Z. X.; Wang, G. F. et al. Atomically dispersed single Ni site catalysts for nitrogen reduction toward electrochemical ammonia synthesis using N_2 and H_2O. *Small Methods* **2020**, *4*, 1900821.

[16] Wang, Y.; Cui, X. Q.; Zhao, J. X.; Jia, G. R.; Gu, L.; Zhang, Q. H.; Meng, L. K.; Shi, Z.; Zheng, L. R.; Wang, C. Y. et al. Rational design of Fe-N/C hybrid for enhanced nitrogen reduction electrocatalysis under ambient conditions in aqueous solution. *ACS Catal.* **2019**, *9*, 336–344.

[17] Qin, Y. Y.; Li, Y.; Zhao, W. S.; Chen, S. H.; Wu, T. T.; Su, Y. Q. Computational study of transition metal single-atom catalysts supported on nitrogenated carbon nanotubes for electrocatalytic nitrogen reduction. *Nano Res.* **2023**, *16*, 325–333.

[18] Senthamaraikannan, T. G.; Lim, D. H. Nitrogen reduction reaction enhanced by single-atom transition metal catalysts on functionalized graphene: A first-principles study. *Int. J. Hydrogen Energy* **2024**, *72*, 449–461.

[19] Le, Y. Q.; Gu, J.; Tian, W. Q. Nitrogen-fixation catalyst based on graphene: Every part counts. *Chem. Commun.* **2014**, *50*, 13319–13322.

[20] Li, X. F.; Li, Q. K.; Cheng, J.; Liu, L. L.; Yan, Q.; Wu, Y. C.; Zhang, X. H.; Wang, Z. Y.; Qiu, Q.; Luo, Y. Conversion of dinitrogen to ammonia by FeN_3-embedded graphene. *J. Am. Chem. Soc.* **2016**, *138*, 8706–8709.

[21] Zhao, J. X.; Chen, Z. F. Single Mo atom supported on defective boron nitride monolayer as an efficient electrocatalyst for nitrogen fixation: A computational study. *J. Am. Chem. Soc.* **2017**, *139*, 12480–12487.

[22] Han, L. L.; Liu, X. J.; Chen, J. P.; Lin, R. Q.; Liu, H. X.; Lü, F.; Bak, S.; Liang, Z. X.; Zhao, S. Z.; Stavitski, E. et al. Atomically dispersed molybdenum catalysts for efficient ambient nitrogen fixation. *Angew. Chem., Int. Ed.* **2019**, *58*, 2321–2325.

[23] Kong, Y.; Wu, L.; Yang, X. X.; Li, Y.; Zheng, S. X.; Yang, B.; Li, Z. J.; Zhang, Q. H.; Zhou, S. D.; Lei, L. C. et al. Accelerating

protonation kinetics for ammonia electrosynthesis on single iron sites embedded in carbon with intrinsic defects. *Adv. Funct. Mater.* **2022**, *32*, 2205409.

[24] Chen, Y.; Guo, R. J.; Peng, X. Y.; Wang, X. Q.; Liu, X. J.; Ren, J. Q.; He, J.; Zhuo, L. C.; Sun, J. Q.; Liu, Y. F. et al. Highly productive electrosynthesis of ammonia by admolecule-targeting single Ag sites. *ACS Nano* **2020**, *14*, 6938–6946.

[25] He, C.; Wu, Z. Y.; Zhao, L.; Ming, M.; Zhang, Y.; Yi, Y. P.; Hu, J. S. Identification of FeN_4 as an efficient active site for electrochemical N_2 reduction. *ACS Catal.* **2019**, *9*, 7311–7317.

[26] Lü, F.; Zhao, S. Z.; Guo, R. J.; He, J.; Peng, X. Y.; Bao, H. L.; Fu, J. T.; Han, L. L.; Qi, G. C.; Luo, J. et al. Nitrogen-coordinated single Fe sites for efficient electrocatalytic N_2 fixation in neutral media. *Nano Energy* **2019**, *61*, 420–427.

[27] Choi, C.; Back, S.; Kim, N. Y.; Lim, J.; Kim, Y. H.; Jung, Y. Suppression of hydrogen evolution reaction in electrochemical N_2 reduction using single-atom catalysts: A computational guideline. *ACS Catal.* **2018**, *8*, 7517–7525.

[28] Liu, X.; Jiao, Y.; Zheng, Y.; Jaroniec, M.; Qiao, S. Z. Building up a picture of the electrocatalytic nitrogen reduction activity of transition metal single-atom catalysts. *J. Am. Chem. Soc.* **2019**, *141*, 9664–9672.

[29] Hu, X.; Chen, S. Y.; Chen, L. T.; Wang, H. J.; Zhang, X.; Zhou, Z. Automating structure–activity analysis for electrochemical nitrogen reduction catalyst design through multi-agent collaborations. *Natl. Sci. Rev.* **2025**, *12*, nwaf372.

[30] Li, R. N.; Ma, R. L.; Zhang, L. L.; Ma, W.; Shao, G. L.; Zhang, X.; Tian, Y.; Jiao, M. G.; Zhou, Z. High-efficiency electrochemical ammonia synthesis at co-catalytic Fe–Mo dual-atom sites. *ACS Nano* **2025**, *19*, 17686–17697.

[31] Lv, K. L.; Teng, C.; Shi, M. H.; Yuan, Y.; Zhu, Y.; Wang, J. R.; Kong, Z.; Lu, X. Y.; Zhu, Y. Hydrophobic and electronic properties of the E-MoS_2 nanosheets induced by FAS for the CO_2 electroreduction to syngas with a wide range of CO/H_2 ratios. *Adv. Funct. Mater.* **2018**, *28*, 1802339.

[32] Luo, Y. J.; Shen, P.; Li, X. C.; Guo, Y. L.; Chu, K. MoS_2 quantum dots for electrocatalytic N_2 reduction. *Chem. Commun.* **2021**, *57*, 9930–9933.

[33] Li, X. H.; Li, T. S.; Ma, Y. J.; Wei, Q.; Qiu, W. B.; Guo, H. R.; Shi, X. F.; Zhang, P.; Asiri, A. M.; Chen, L. et al. Boosted electrocatalytic N_2 reduction to NH_3 by defect-rich MoS_2 nanoflower. *Adv. Energy Mater.* **2018**, *8*, 1801357.

[34] Tsai, C.; Li, H.; Park, S.; Park, J.; Han, H. S.; Nørskov, J. K.; Zheng, X. L.; Abild-Pedersen, F. Electrochemical generation of sulfur vacancies in the basal plane of MoS_2 for hydrogen evolution. *Nat. Commun.* **2017**, *8*, 15113.

[35] Fei, H.; Liu, R. Q.; Wang, J.; Guo, T.; Wu, Z. Z.; Wang, D. Z.; Liu, F. Y. Targeted modulation of competitive active sites toward nitrogen fixation via sulfur vacancy engineering over MoS_2. *Adv. Funct. Mater.* **2023**, *33*, 2302501.

[36] Wang, X.; Zhang, Y. W.; Si, H. N.; Zhang, Q. H.; Wu, J.; Gao, L.; Wei, X. F.; Sun, Y.; Liao, Q. L.; Zhang, Z. et al. Single-atom vacancy defect to trigger high-efficiency hydrogen evolution of MoS_2. *J. Am. Chem. Soc.* **2020**, *142*, 4298–4308.

[37] Dang, Q.; Tang, S. B.; Liu, T. Y.; Li, X. K.; Wang, X. J.; Zhong, W. H.; Luo, Y.; Jiang, J. Regulating electronic spin moments of single-atom catalyst sites via single-atom promoter tuning on S-vacancy MoS_2 for efficient nitrogen fixation. *J. Phys. Chem. Lett.* **2021**, *12*, 8355–8362.

[38] Zhang, J.; Tian, X. Y.; Liu, M. J.; Guo, H.; Zhou, J. D.; Fang, Q. Y.; Liu, Z.; Wu, Q.; Lou, J. Cobalt-modulated molybdenum–dinitrogen interaction in MoS_2 for catalyzing ammonia synthesis. *J. Am. Chem. Soc.* **2019**, *141*, 19269–19275.

[39] Jiang, Z. Z.; Zhou, W. D.; Hu, C.; Luo, X. F.; Zeng, W.; Gong, X. G.; Yang, Y.; Yu, T.; Lei, W.; Yuan, C. L. Interlayer-confined NiFe dual atoms within MoS_2 electrocatalyst for ultra-efficient acidic overall water splitting. *Adv. Mater.* **2023**, *35*, 2300505.

[40] Wang, T.; Abild-Pedersen, F. Achieving industrial ammonia synthesis rates at near-ambient conditions through modified scaling relations on a confined dual site. *Proc. Natl. Acad. Sci. USA* **2021**, *118*, e2106527118.

[41] Liu, C. L.; Xu, G. M.; Wang, T. Theoretical approach toward a mild condition Haber–Bosch process on the zeolite catalyst with confined dual active sites. *JACS Au* **2023**, *3*, 3374–3380.

[42] Chen, Z.; Liu, Y. H.; Wang, T. Steering competitive N_2 and CO adsorption toward efficient urea production with a confined dual site. *Chem. Sci.* **2023**, *14*, 12707–12714.

[43] Zhao, W. H.; Xu, G. M.; He, Z. C.; Cai, C.; Abild-Pedersen, F.; Wang, T. Toward carbon monoxide methanation at mild conditions on dual-site catalysts. *J. Am. Chem. Soc.* **2023**, *145*, 8726–8733.

[44] Huang, D. L.; Shao, G. L.; Zhang, X.; Zhou, Z. Electronic mechanism behind the influence of intercalated heteroatom Sn on the slip energy barrier in layered WS_2. *Nanotechnology* **2025**, *36*, 225201.

[45] Kresse, G.; Hafner, J. *Ab initio* molecular dynamics for liquid metals. *Phys. Rev. B* **1993**, *47*, 558–561.

[46] Perdew, J. P.; Wang, Y. Accurate and simple analytic representation of the electron-gas correlation energy. *Phys. Rev. B* **1992**, *45*, 13244–13249.

[47] Perdew, J. P.; Burke, K.; Ernzerhof, M. Generalized gradient approximation made simple. *Phys. Rev. Lett.* **1996**, *77*, 3865–3868.

[48] Grimme, S. Semiempirical GGA-type density functional constructed with a long-range dispersion correction. *J. Comput. Chem.* **2006**, *27*, 1787–1799.

[49] Henkelman, G.; Arnaldsson, A.; Jónsson, H. A fast and robust algorithm for Bader decomposition of charge density. *Comput. Mater. Sci.* **2006**, *36*, 354–360.

[50] Sanville, E.; Kenny, S. D.; Smith, R.; Henkelman, G. Improved grid-based algorithm for Bader charge allocation. *J. Comput. Chem.* **2007**, *28*, 899–908.

[51] Henkelman, G.; Uberuaga, B. P.; Jónsson, H. A climbing image nudged elastic band method for finding saddle points and minimum energy paths. *J. Chem. Phys.* **2000**, *113*, 9901–9904.

[52] Nørskov, J. K.; Rossmeisl, J.; Logadottir, A.; Lindqvist, L.; Kitchin, J. R.; Bligaard, T.; Jónsson, H. Origin of the overpotential for oxygen reduction at a fuel-cell cathode. *J. Phys. Chem. B* **2004**, *108*, 17886–17892.

[53] Skúlason, E.; Tripkovic, V.; Björketun, M. E.; Gudmundsdóttir, S.; Karlberg, G.; Rossmeisl, J.; Bligaard, T.; Jónsson, H.; Nørskov, J. K. Modeling the electrochemical hydrogen oxidation and evolution reactions on the basis of density functional theory calculations. *J. Phys. Chem. C* **2010**, *114*, 22374.

[54] Johnson III, R. D. NIST computational chemistry comparison and benchmark database NIST standard reference database number 101 [Online]. http://cccbdb.nist.gov/ (accessed May 22, 2022).

[55] Mathew, K.; Kolluru, V. S. C.; Mula, S.; Steinmann, S. N.; Hennig, R. G. Implicit self-consistent electrolyte model in plane-wave density-functional theory. *J. Chem. Phys.* **2019**, *151*, 234101.

[56] Mathew, K.; Sundararaman, R.; Letchworth-Weaver, K.; Arias, T. A.; Hennig, R. G. Implicit solvation model for density-functional study of nanocrystal surfaces and reaction pathways. *J. Chem. Phys.* **2014**, *140*, 084106.

[57] Chu, K.; Liu, Y. P.; Li, Y. B.; Guo, Y. L.; Tian, Y. Two-dimensional (2D)/2D interface engineering of a MoS_2/C_3N_4 heterostructure for promoted electrocatalytic nitrogen fixation. *ACS Appl. Mater. Interfaces* **2020**, *12*, 7081–7090.

[58] Chen, Z.; Zhao, J. X.; Cabrera, C. R.; Chen, Z. F. Computational screening of efficient single-atom catalysts based on graphitic carbon nitride (g-C_3N_4) for nitrogen electroreduction. *Small Methods* **2019**, *3*, 1800368.

[59] Chen, Z.; Zhao, J. X.; Jiao, Y.; Wang, T.; Yin, L. C. Achieving efficient N_2 electrochemical reduction by stabilizing the N_2H^* intermediate with the frustrated lewis pairs. *J. Energy Chem.* **2022**, *66*, 628–634.

[60] Deng, J.; Iñiguez, J. A.; Liu, C. Electrocatalytic nitrogen reduction at low temperature. *Joule* **2018**, *2*, 846–856.
[61] Zhao, J.; Zhao, J. X.; Cai, Q. H. Single transition metal atom embedded into a MoS_2 nanosheet as a promising catalyst for electrochemical ammonia synthesis. *Phys. Chem. Chem. Phys.* **2018**, *20*, 9248–9255.
[62] Chu, K.; Liu, Y. P.; Cheng, Y. H.; Li, Q. Q. Synergistic boron-dopants and boron-induced oxygen vacancies in MnO_2 nanosheets to promote electrocatalytic nitrogen reduction. *J. Mater. Chem. A* **2020**, *8*, 5200–5208.
[63] Aras, M.; Kılıç, Ç.; Ciraci, S. Lateral and vertical heterostructures of transition metal dichalcogenides. *J. Phys. Chem. C* **2018**, *122*, 1547–1555.
[64] Chaitoglou, S.; Giannakopoulou, T.; Tsoutsou, D.; Vavouliotis, A.; Trapalis, C.; Dimoulas, A. Direct versus reverse vertical two-dimensional Mo_2C/graphene heterostructures for enhanced hydrogen evolution reaction electrocatalysis. *Nanotechnology* **2019**, *30*, 415404.
[65] Liu, Y. D.; Chen, Y.; Tian, Y. H.; Sakthivel, T.; Liu, H.; Guo, S. W.; Zeng, H. B.; Dai, Z. F. Synergizing hydrogen spillover and deprotonation by the internal polarization field in a MoS_2/$NiPS_3$ vertical heterostructure for boosted water electrolysis. *Adv. Mater.* **2022**, *34*, 2203615.
[66] Zhang, Y. J.; Wang, X. K.; Song, X. J.; Jiang, H. Q. Collaborative effect between single-atom Re and S vacancy on modulating localized electronic structure of MoS_2 catalysts for alkaline hydrogen evolution. *Nano Res.* **2024**, *17*, 9507–9517.
[67] Chee, S. S.; Oh, C.; Son, M.; Son, G. C.; Jang, H.; Yoo, T. J.; Lee, S.; Lee, W.; Hwang, J. Y.; Choi, H. et al. Sulfur vacancy-induced reversible doping of transition metal disulfides via hydrazine treatment. *Nanoscale* **2017**, *9*, 9333–9339.
[68] Yue, S.; Zhao, Z. Y.; Liu, Y. X.; Yang, M. X.; Zhang, T.; Li, F.; Liu, K. W.; Wang, P. F.; Zhan, S. H. Dual-site synergistic electrocatalysis enables highly selective upcycling of real-world plastic waste to glycolic acid. *Adv. Funct. Mater.* **2025**, *35*, 09766.
[69] Seh, Z. W.; Kibsgaard, J.; Dickens, C. F.; Chorkendorff, I.; Nørskov, J. K.; Jaramillo, T. F. Combining theory and experiment in electrocatalysis: Insights into materials design. *Science* **2017**, *355*, eaad4998.
[70] Xu, L. T.; Huang, Y. H.; Lin, H. P.; Du, R. H.; Wang, M.; Ma, F.; Wei, X. M.; Zhu, G. Q.; Zhang, J. M. High-throughput screening of carbon nitride single-atom catalysts for nitrogen fixation based on machine learning. *J. Mater. Chem. A* **2024**, *12*, 33053–33065.
[71] Guo, X. Y.; Gu, J. X.; Lin, S. R.; Zhang, S. L.; Chen, Z. F.; Huang, S. P. Tackling the activity and selectivity challenges of electrocatalysts toward the nitrogen reduction reaction via atomically dispersed biatom catalysts. *J. Am. Chem. Soc.* **2020**, *142*, 5709–5721.
[72] Chang, X.; Zhao, Z. J.; Lu, Z. P.; Chen, S.; Luo, R.; Zha, S. J.; Li, L. L.; Sun, G. D.; Pei, C. L.; Gong, J. L. Designing single-site alloy catalysts using a degree-of-isolation descriptor. *Nat. Nanotechnol.* **2023**, *18*, 611–616.
[73] Ren, C. J.; Lu, S. H.; Wu, Y. L.; Ouyang, Y. X.; Zhang, Y. H.; Li, Q.; Ling, C. Y.; Wang, J. L. A universal descriptor for complicated interfacial effects on electrochemical reduction reactions. *J. Am. Chem. Soc.* **2022**, *144*, 12874–12883.
[74] Xu, M. M.; Ji, Y. J.; Qin, Y. Y.; Dong, H. L.; Li, Y. Y. A universal descriptor for two-dimensional carbon nitride-based single-atom electrocatalysts towards the nitrogen reduction reaction. *J. Mater. Chem. A* **2024**, *12*, 28046–28055.
[75] Wen, Z. L.; Lv, H. F.; Wu, D. X.; Zhang, W. H.; Wu, X. J.; Yang, J. L. Sulfur-coordinated transition metal atom in graphene for electrocatalytic nitrogen reduction with an electronic descriptor. *J. Phys. Chem. Lett.* **2022**, *13*, 8177–8184.
[76] Nie, X. W.; Esopi, M. R.; Janik, M. J.; Asthagiri, A. Selectivity of CO_2 reduction on copper electrodes: The role of the kinetics of elementary steps. *Angew. Chem., Int. Ed.* **2013**, *52*, 2459–2462.
[77] Skúlason, E.; Bligaard, T.; Gudmundsdóttir, S.; Studt, F.; Rossmeisl, J.; Abild-Pedersen, F.; Vegge, T.; Jónsson, H.; Nørskov, J. K. A theoretical evaluation of possible transition metal electro-catalysts for N_2 reduction. *Phys. Chem. Chem. Phys.* **2012**, *14*, 1235–1245.
[78] Montoya, J. H.; Tsai, C.; Vojvodic, A.; Nørskov, J. K. The challenge of electrochemical ammonia synthesis: A new perspective on the role of nitrogen scaling relations. *ChemSusChem* **2015**, *8*, 2180–2186.
[79] Yan, Y.; Liang, S.; Wang, X.; Zhang, M. Y.; Hao, S. M.; Cui, X.; Li, Z. W.; Lin, Z. Q. Robust wrinkled MoS_2/N–C bifunctional electrocatalysts interfaced with single Fe atoms for wearable zinc-air batteries. *Proc. Natl. Acad. Sci. USA* **2021**, *118*, e2110036118.